Electrochemical processes of nucleation and growth of calcium phosphate on titanium supported by real-time quartz crystal microbalance measurements and X-ray photoelectron spectroscopy analysis

Noam Eliaz,[1] William Kopelovitch,[1] Larisa Burstein,[2] Equo Kobayashi,[3] Takao Hanawa[3]
[1]*Biomaterials and Corrosion Laboratory, School of Mechanical Engineering, Tel Aviv University, Ramat Aviv 69978, Israel*
[2]*The Wolfson Applied Materials Research Centre, Tel Aviv University, Ramat Aviv 69978, Israel*
[3]*Institute of Biomaterials and Bioengineering, Tokyo Medical and Dental University, Tokyo 101-0062, Japan*

Received 22 June 2007; revised 2 April 2008; accepted 2 April 2008
Published online 18 June 2008 in Wiley InterScience (www.interscience.wiley.com). DOI: 10.1002/jbm.a.32129

Abstract: Real-time, *in situ* electrochemical quartz crystal microbalance (EQCM) measurements are conducted to better understand the electrocrystallization of calcium phosphates (CaP) on CP-Ti. X-ray photoelectron spectroscopy is used to identify the exact phase deposited, so that reliable estimation of the electrochemical processes involved is made. Analysis of the integrated intensity of the oxygen shake-up peaks, in combination with the determination of Ca/P and O/Ca atomic ratios, enables to determine unambiguously that the octacalcium phosphate (OCP) is formed. Its role as a precursor to hydroxyapatite (HAp) is discussed. After an incubation period, the process by which OCP is formed follows a Faradaic behavior. The incubation time may be related to the need for local increase of pH before precipitation from solution can occur. The standard enthalpy of activation is ~40 kJ/mol, which excludes diffusion-controlled processes from being rate determining. The OCP deposit has thickness $\approx$ 0.61 μm, apparent density $\approx$ 0.95 g/cm^3, 63.6% porosity, and deposition rate of 23.5 ng/(cm^2 s) or 15 nm/min. The low-equivalent weight value of 20.5 g/equiv, and the associated remarkably high number of electrons transferred in the reaction $n \approx 24$, indicates that most of the current is consumed either by electrolysis of water or by a complex set of parasitic reactions. The low-solubility product allows precipitation of CaP even at relatively low concentrations of calcium and phosphate/hydrogen phosphate ions. It is shown that HAp most likely forms via transformation of precursor phases, such as OCP, rather than directly. © 2008 Wiley Periodicals, Inc. J Biomed Mater Res 89A: 270–280, 2009

Key words: calcium phosphate; titanium; electrodeposition; quartz crystal microbalance; XPS

INTRODUCTION

Apatite is the major inorganic constituent of enamel, dentin, and vertebrate bone. It belongs to the family of calcium phosphates (CaP), which includes, among others, hydroxyapatite (HAp), α- and β-tricalcium phosphates (TCP), octacalcium phosphate (OCP), dibasic calcium phosphate dihydrate (DCPD or brushite), dibasic calcium phosphate anhydrous (DCPA or monetite), monobasic calcium phosphate monohydrate (MCPM), and amorphous calcium phosphate (ACP).[1,2] Synthetic CaP coatings are more bioactive and osteoconductive compared to metal surfaces and form direct bonds with adjacent hard tissues. Hence, apatite coatings, mostly plasma sprayed, are often applied on implants when good osseointegration is desired. Nevertheless, loosening of implants has been reported during long-term service, that is, from several months to several years, depending on the properties of the coating.[3–6] The interest in electrochemical deposition has increased in the recent years due to the inherent advantages of this process, as summarized earlier.[7–10]

A better understanding of the electrochemical processes that take part in deposition of HAp is important from a technological point of view, namely the ability to form coatings with enhanced properties on orthopedic and dental implants. Furthermore, because electrochemical (and chemical) processes have been proven successful in producing biomimetic CaP coatings, the analogy to processes that may take place *in vivo* could improve our understanding of

Correspondence to: N. Eliaz; e-mail: neliaz@eng.tau.ac.il

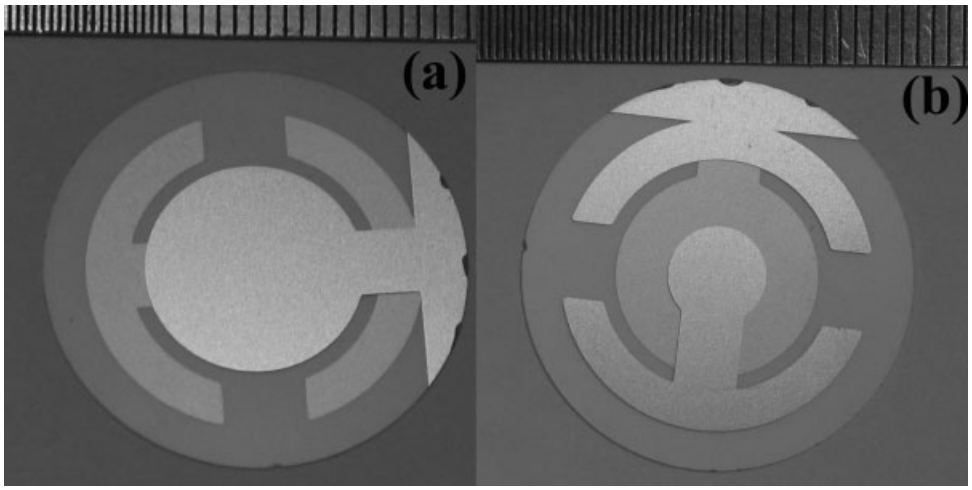

Figure 1. The upper side (a) and bottom side (b) of the Ti-coated quartz plate.

biomineralization, and how it may be controlled. The electrochemical quartz crystal microbalance (EQCM) is a powerful method that can be applied for this purpose. The correlation between the measured frequency change Δf and the elastic mass change Δm is expressed via the Sauerbrey Equation[11]:

$$\Delta f = -\frac{2f_0^2 \Delta m}{A^* \sqrt{\rho_q \mu_q}} \tag{1.1}$$

where f_0 is the resonance frequency of the oscillating quartz crystal (QC) prior to the mass change (6 MHz in this study), A^* is the piezoelectrically active area, ρ_q and μ_q are the density and the shear modulus of the QC (2.648 g/cm^3 and 2.947 $\times$ 10^{10} N/m^2, respectively). Thus, Eq. (1.1) may be rewritten as

$$\frac{\Delta m}{A^*}\left(\text{ng/cm}^2\right) = -12.27 \Delta f(\text{Hz}) \tag{1.2}$$

The high sensitivity and the real-time monitoring of mass changes on the sensor crystal make the QCM a very attractive technique for a large range of applications. The EQCM also enables the application of potential on the upper metal electrode, thereby creating an electrochemical cell and allowing electrochemical reactions or measurement of processes involving charge transfer.[12–19] EQCM measurements provide a very sensitive means for the determination of equivalent weight (EW), based on the following equation[20]:

$$\text{EW} \equiv \frac{M}{n} = \frac{F \Delta m}{A^* \Delta Q} \tag{2}$$

where M is the molar mass (g/mol), n is the number of electrons transferred (equiv/mol), F is Faraday's constant (96,485 C/equiv), $\Delta m/A^*$ is given in units of gram per centimeter square, and ΔQ is the charge density (C/cm^2). Thus, the EW can be deduced from the slope of the line $\Delta m/A^*$ versus ΔQ.

In spite of the important mechanistic information that may be extracted from QCM data, the use of this method in studying the chemical or electrochemical deposition of CaP has been very narrow so far.[21–30] Even in these few papers, the extent to which new, significant knowledge was extracted from the QCM measurements, was fairly limited. This is because (1) QCM was used to measure the mass gain and the related deposition kinetics, with no attempt to identify the reactions involved; (2) the exact chemical composition of the CaP phase was either hypothesized or measured with some ambiguity; and (3) the thickness of the deposit was calculated in two cases based on the QCM data and the theoretical density of HAp,[27,30] instead of using complementary techniques.

The objective of this work is to extend the work of Eliaz and Eliyahu[7] and use real-time, *in situ* EQCM measurements to better understand the electrocrystallization of CaP on CP-Ti, focusing on the short-term deposition. From Eq. (2), it is evident that in order to determine the number of electrons transferred in the reaction the exact molecular mass of the mineral deposited on the surface must be identified. To this aim, we use advanced, surface-sensitive X-ray photoelectron spectroscopy (XPS) analysis.

EXPERIMENTAL

The EQCM apparatus for real-time deposition experiments consists of a frequency counter (HQ-101B controller), a computer-controlled potentiostat/galvanostat (HZ-3000), and a cell (HQ-305A mass sensor), all from Hokuto Denko, Japan. A QC element (AT-cut, 6 MHz) coated with pure Ti is used as the working electrode. The upper metal electrode [Fig. 1(a)] has a diameter d = 1.3 cm and an effective surface area A = 1.327 cm^2. The upper side of the electrode is sealed with an O-ring, so that the bottom side [Fig. 1(b)] remains dry and provides a two-point short-circuit to the mass sensor. The cell contains 30 mL of the electrolyte solution. The latter is prepared by dissolving

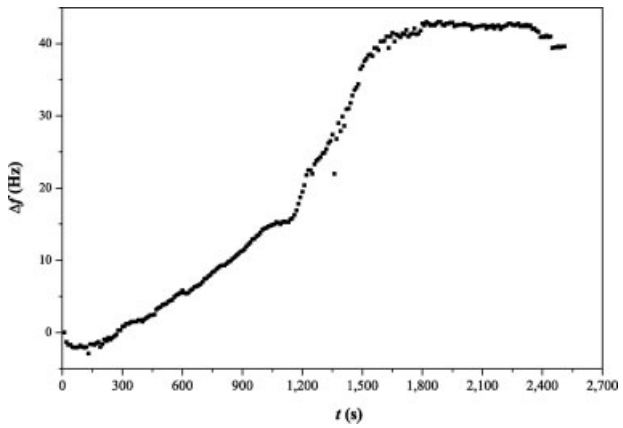

Figure 2. The change in frequency during a stability test, that is, in the absence of applied potential.

0.61 m*M* $Ca(NO_3)_2$ and 0.36 m*M* $NH_4H_2PO_4$ (AR-grade, Wako Pure Chemical Industries) in Milli-DI^{TM} water (Millipore). The pH is adjusted to 6.0 by the addition of 0.1*M* NaOH and measured before the experiment starts by HM-60V pH meter (DKK-TOA). The bath composition and pH values are chosen so as to enable formation of HAp based on solubility isotherms for CaP.[31] A platinum counter electrode is electrically connected to one side of the mass sensor. A standard SCE reference electrode is immersed in the electrolyte. A potentiostatic mode is used, setting the cathode potential at −1.29 V versus SCE for 40 min. Neither purging nor stirring is carried out during the experiment. The bath temperature is fixed at 65°C ± 0.1°C.

An electrode resonance stability experiment is carried out prior to the electrodeposition experiment. The complete setup (i.e., mass sensor, electrode, and electrolyte solution) is first placed inside a thermostatic bath. Twenty minutes after reaching the desired bath temperature (65°C), the stability experiment begins, and the variation in frequency is monitored for nearly 40 min in the absence of applied potential. The electrodeposition experiment itself starts immediately (∼1 s) after applying potential to the cell. The preset parameters include fundamental frequency of 6,032,920 Hz, deposition time of 40 min, and data acquisition rate of 10 points per second.

The titanium electrode is imaged in a desk-top SEM (TM-1000 Mini-Scope, Hitachi) before and after deposition to ensure that a deposit actually formed on the surface. The surface morphology, thickness, and chemical composition of the deposit are later characterized also by ESEM (Quanta 200 FEG, FEI), equipped with an Oxford INCA energy dispersive spectroscopy (EDS) system. A PicoSPM^{TM} (Molecular Imaging) EC-AFM is used to characterize the surface morphology of the CaP deposit *ex situ*. Imaging is done under contact mode using tips made of Si_3N_4 (Veeco). Both topography and deflection (error signal) images are acquired. The mean length and mean width of the CaP crystals are determined by direct measurement of features on the deflection image. The mean thickness, on the other hand, is determined from line scans on the topography image.

XPS measurements are performed in UHV (2.5×10^{-10} Torr base pressure), using a 5600 Multi-Technique System (PHI, USA). The sample is irradiated with an Al Kα monochromated source (1486.6 eV), and the outcome electrons are analyzed by a hemispherical analyzer, using a slit aperture of 0.8 mm in diameter. Charging is compensated with charge neutralizer. The binding energy (BE) of adventitious carbon at 285 eV is taken as an energy reference for all measured peaks. A low-resolution survey spectrum is taken over a wide energy range (0–1400 eV) to identify the elements present at the sample surface. High-resolution spectra are taken at pass energy of 11.75 eV at an increment of 0.05 eV/step. The atomic ratios Ca/P and O/Ca are determined from these measurements.

RESULTS

Figure 2 presents the time dependence of the measured frequency change during the stability test. Ideally, the frequency change is expected to equal zero through such an experiment if no changes occur at the surface of the electrode and in the adjacent solution during immersion. However, a positive shift of ∼40 Hz is monitored here. This shift is several orders of magnitude smaller than the change in frequency measured during the subsequent electrodeposition experiment. In addition, for the last 10 min of the stability test, the frequency change is negligible. Thus, it may be concluded that the system properly reached stability, and that the frequency change monitored during the electrodeposition experiment itself truly reflects the electrochemical processes that take place.

Figure 3 presents the potentiostatic current transient and the related time-dependence of the accumulated charge density ΔQ (mC/cm^2) during the electrodeposition experiment. It follows that ΔQ is about 272 mC/cm^2 at the end of the experiment. During the first 11 min, the ΔQ versus time curve is nonlinear, and the charge values are higher than

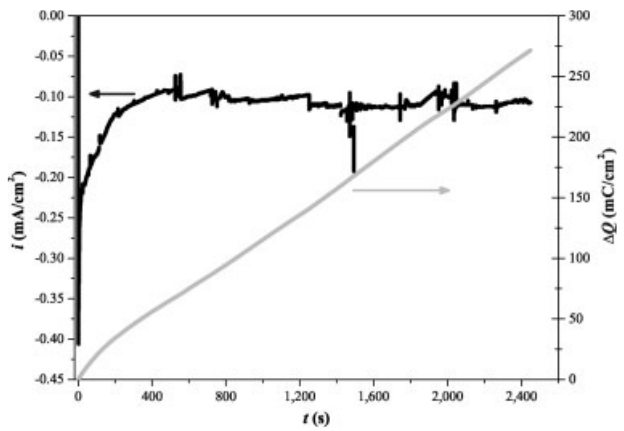

Figure 3. The potentiostatic cathodic current transient and the related time dependence of accumulated charge density during electrodeposition of CaP on an EQCM electrode.

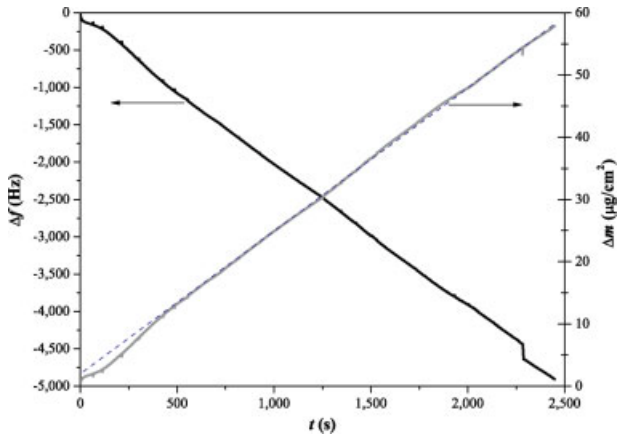

Figure 4. The time dependence of frequency change and mass gain, the latter calculated using Eq. (1.2). [Color figure can be viewed in the online issue, which is available at www.interscience.wiley.com.]

those extrapolated from the linear regime. Then, however, ΔQ increases linearly with time. The slope of the line is $\sim$107.5 μC/(cm^2 s). This linear relation, in combination with the linear time dependence of the mass gain (see Fig. 4), indicates that a Faradaic, namely charge transfer, reaction is taking place. The current transient in Figure 3 consists of three egimes: (1) rapid current rise (to –0.41 mA/cm^2 in 1.5 s), (2) current decay for $\sim$11 min, and (3) current stabilization at around -0.1 mA/cm^2. Applying linearization procedures on the experimental data, by means of the Cottrell equation ($i = 1/t^{1/2}$) or the exponential law $i = \exp(-kt)$, does not reveal any linear relationship. This result indicates that the CaP nucleation process is not diffusion-controlled.

Figure 4 shows the measured frequency change and the corresponding mass gain, as calculated by the Sauerbrey Eq. (1.2). The dashed line illustrates that, except during the first 7.3 min or so, the mass increases linearly with time. As explained earlier, this is characteristic of a Faradaic reaction. Linear curve-fitting results in the following relation between mass gain and time:

$$\Delta m = 0.0235t + 1.024, \quad R^2 = 0.9994 \qquad (3)$$

where R^2 is the determination coefficient. This means that the growth rate (slope) is 23.5 ng/(cm^2 s). If we divide this value by the slope of ΔQ versus t in the linear regime, we get 218.6 μg/C.

During the first 7.3 min, the mass gain is not linear, and its values are lower than those extrapolated from the linear regime. This initial behavior may be a sign of some sort of incubation time, for example, due to the need for the pH in vicinity of the working electrode to increase above a certain limit. Curve fitting (not included herein) shows that during the first 115 s, the growth rate is approximately half that during the overall experiment. Note that the incubation time observed herein by monitoring of Δm is shorter than the time period during which ΔQ deviates from linearity. It should be emphasized that the current density and the frequency change are monitored independently; therefore, the time dependencies of ΔQ and Δm are calculated separately too. Hence, it may be concluded that during the earliest 11 min of deposition, at least two different processes are monitored by the EQCM measurements, for example, the effect of local increase of the pH and the nucleation of a precursor with lower mass density and higher charge density.

To better evaluate the characteristics of the deposit, SEM and ESEM images of both the top surface and cross-section are acquired. Figure 5(a,b) shows SEM top view of uncoated and coated regions, respectively. Comparing these two images, it is evident that a thin deposit actually formed on the surface of the electrode. In the cross-section [ESEM, Fig. 5(c)], three layers can be distinguished: (1) thick quartz substrate at the bottom, (2) Ti (white) layer in the middle—about 0.19 ± 0.01 μm thick, and (3) top deposit layer, $\sim$0.61 ± 0.13 μm thick. The deposit is found to be well adherent to the surface and exhibits surface morphology of needles. This latter finding is similar to the previous observations.[7] AFM images (Fig. 6) reveal platelets of CaP that grow in preferred orientation, while accumulating within domains. The length, width, and thickness of each CaP platelet are $\sim$0.44, 0.20, and 0.10 μm, respectively. These dimensions are significantly higher than those reported by Eliaz and Eliyahu for 2D growth of Hap, whereas the crystal morphology is different from that observed during 3D growth of HAp.[7]

EDS analysis reveals a Ca/P atomic ratio of nearly 1.0 in this work, when excluding all other elements from the analysis (i.e., Ca + P = 100%). This ratio is much lower than that in HAp, but is equal to the ratio typical of DCPD, DCPA, calcium pyrophosphate (CPP), or calcium pyrophosphate dehydrate (CPPD). However, as will be shown below, such an EDS analysis is not reliable. It should be noted that X-ray mapping of the cross-section is also undertaken inside the ESEM, but fails due to intermixing of signals from different layers. Hence, to proceed with the analysis of the EQCM data, it becomes crucial to identify the exact CaP formed on the Ti electrode. To this aim, XPS analyses are used. A representative low-resolution survey spectrum is shown in Figure 7. Besides, the expected Ca, P, and O peaks, Ti, and C peaks are also evident. The presence of the Ti peaks indicates that the CaP coating is either thin compared to the electron escape depth or very porous. The observed Ti(2p) peak at $\sim$459 eV is characteristic of the titanium dioxide and reflects an oxi-

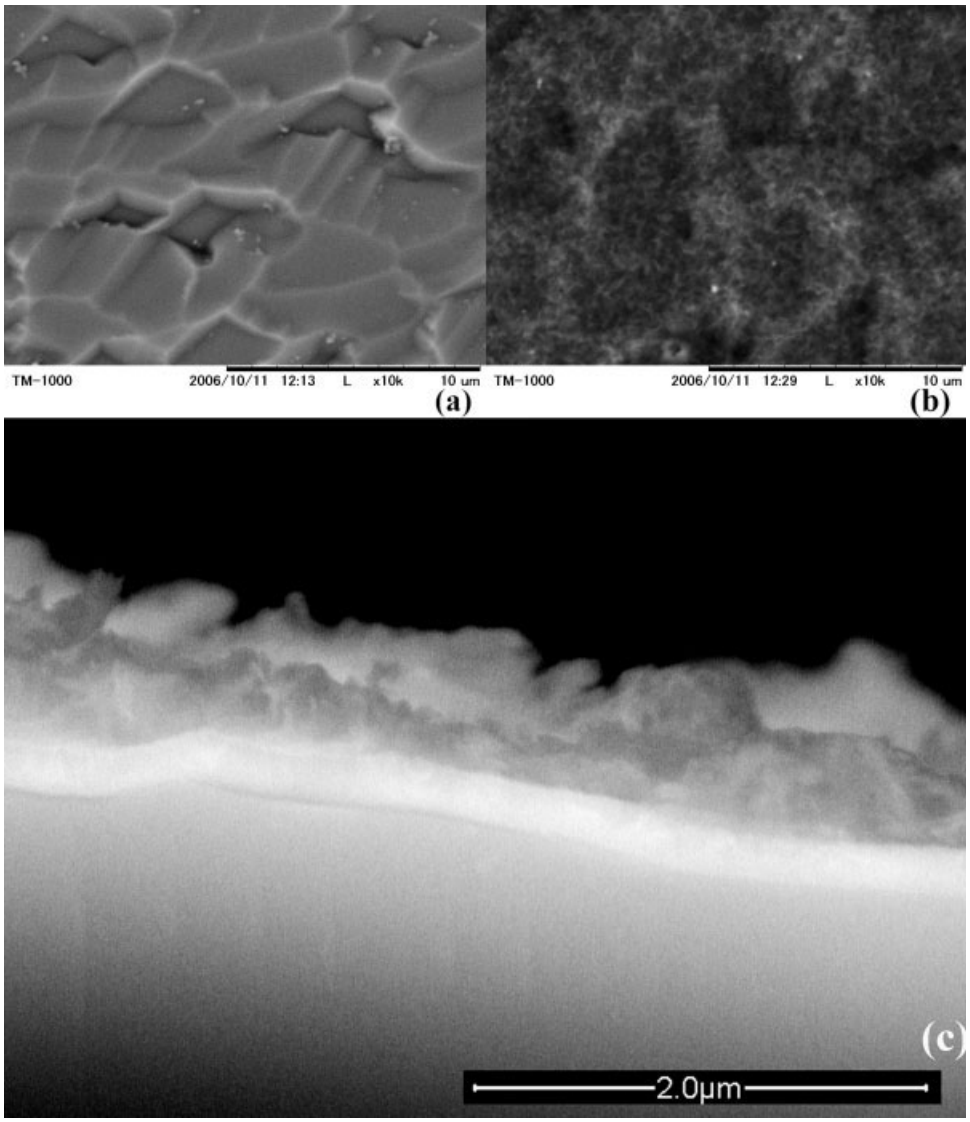

Figure 5. SEM/ESEM secondary electron images: (a) top view of an uncoated region, (b) top view of a coated region, and (c) cross-section, exposing the CaP, Ti, and quartz layers (top to bottom).

dized substrate surface. High-resolution scans (not included herein) reveal the following peak positions: P(2p) at 133.00 eV, Ca(2p) at 347.05 eV, and O(1s) at 531.00 eV. The C(1s) peak at 285 eV is related to hydrocarbon impurities ("adventitious carbon") and used for BE calibration. The high-resolution measurement of the carbon C(1s) structure (not presented herein) indicates that the coating is free of the carbonate-type carbon ($BE \sim 289.3$ eV), an impurity that is often incorporated into synthetic CaP due to the presence of CO_2 in the air or in solution. Angle-resolved XPS measurements, not performed herein, may further support this observation. The absence of the carbonate species allows to present the atomic ratios of elements as measured, with no adjustment, unlike those made in the work of Lu et al.[32] The atomic concentration of elements obtained from high-resolution measurements is given in Table I, together with the Ca/P and O/Ca atomic ratios. The measured Ca/P ratio is more similar to the characteristic of OCP. It is thus evident that the use of EDS data for determining the Ca/P ratio might have led to a wrong conclusion. Yet, it should be mentioned here that the measured Ca/P atomic ratio, obtained from conventional XPS analysis, has been found to be always lower than the theoretical value for different CaP on the surface, thus preventing their unambiguous identification.[32,33]

For further support in relating the CaP phase to OCP, the oxygen loss spectrum is analyzed. Figures 8 and 9 depict the core level O(1s) peak at 531.00 eV and the associated $O(1s)_I$ and $O(1s)_{II}$ shake-up satellite structures at ~553.10 and ~566.60 eV, respectively. It has been reported that the integrated intensity (i.e., peak area) of the shake-up peaks is closely related to different functional groups such as O—H

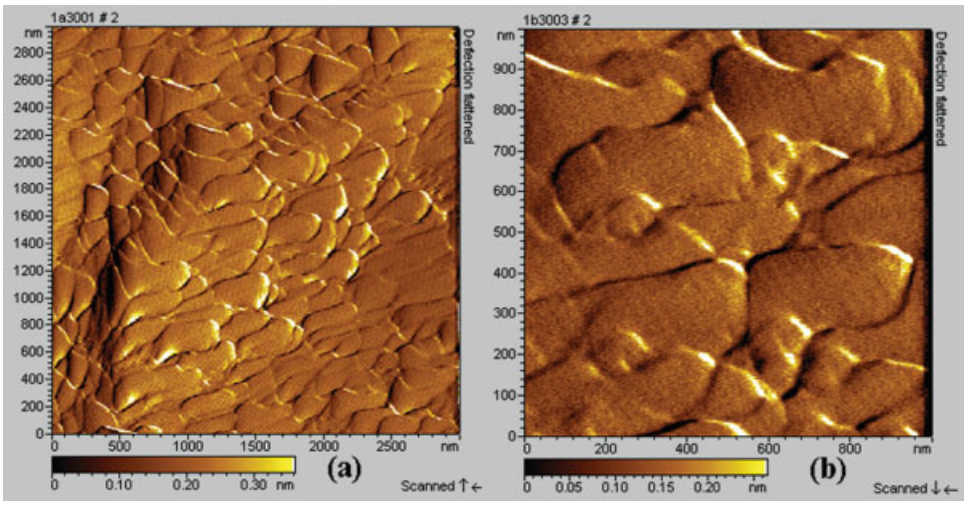

Figure 6. AFM deflection mode images of the CaP coating at different magnifications: (a) 3000 × 3000 nm^2 and (b) 1000 × 1000 nm^2. [Color figure can be viewed in the online issue, which is available at www.interscience.wiley.com.]

and P=O.[32,33] Hence, two different normalization approaches have been used. In one case, the integrated intensity of $O(1s)_{II}$ was divided by the total O(1s) intensity (i.e., by the sum of the main core level peak, $O(1s)_I$ and $O(1s)_{II}$).[32] In the second case, the sum of the areas underneath both $O(1s)_I$ and $O(1s)_{II}$ was divided by the total O(1s) intensity.[33] In this work, both approaches are tested. However, the first approach yields clearer phase identification and is thus presented in this work. We use Shirley baseline subtraction followed by Gaussian curve fitting to calculate the integrated intensities of the O(1s), $O(1s)_I$, and $O(1s)_{II}$ peaks. The areas calculated this way are A_0 = 30,433, A_I = 2683, and A_{II} = 2091 counts/s, respectively (see Fig. 9). The integrated intensity of $O(1s)_{II}$ normalized by the total $O(1s)_{total}$ intensity results in a value of 0.059. Table II compares the Ca/P, O/Ca, and $O(1s)_{II}/O(1s)_{total}$ values measured in this study to those reported by Lu et al.[32] From this comparison, it may be concluded with high level of confidence that the CaP phase, which has been electrodeposited on the EQCM electrode, is indeed OCP. It should be noted that calculations such as those made by Lu et al. to determine the relative contents of different CaP phases are not applicable to thin coatings on substrates, because some of the oxygen signal may be associated with an oxide on the surface of the substrate and not only from the CaP phases and carbonate contamination (if exists).

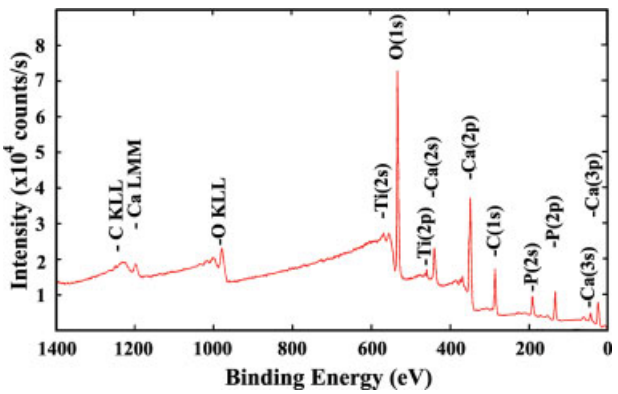

Figure 7. A representative low-resolution XPS survey spectrum, which shows the element composition of the electrodeposited CaP coating on top of the Ti/quartz EQCM electrode. [Color figure can be viewed in the online issue, which is available at www.interscience.wiley.com.]

Realizing that the coating on the Ti electrode is made of OCP, we may now continue analyzing the EQCM data accordingly. Taking into account the thickness of the coating (0.61 μm), as measured by ESEM, and the mass gain at the end of the experiment (57.9 $\mu g/cm^2$), the apparent density of the OCP coating is 0.95 g/cm^3. The theoretical density of OCP is 2.61 g/cm^3;[1] therefore, the porosity level may be estimated as follows:

$$\text{Porosity} = \left(1 - \frac{0.95}{2.61}\right) \times 100 = 63.6\% \qquad (4)$$

TABLE I
Chemical Composition of the CaP Deposit on Top of the Ti EQCM Electrode, as Determined by High-Resolution XPS Scans

Element	At. %
O	46.69
Ca	14.76
P	11.81
C	26.74
Ca/P	1.25
O/Ca	3.16

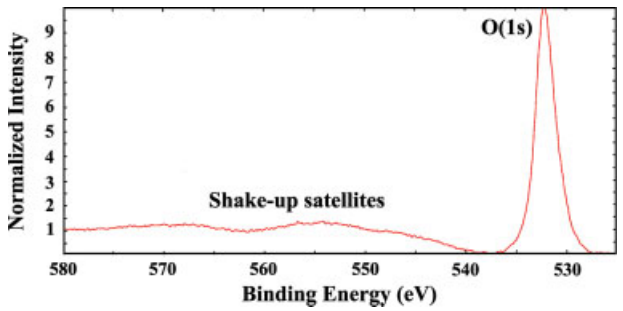

Figure 8. High-resolution XPS scan, which shows the core level peak of O(1s) and the associated satellite structure. [Color figure can be viewed in the online issue, which is available at www.interscience.wiley.com.]

This high porosity should be beneficial for orthopedic and dental implants, as it would allow cell invasion and bone ingrowth. It is directly evident from top view ESEM images and indirectly by the fact that a peak from the TiO_2 substrate was detected by XPS analysis, even without sputtering. As the mass gain versus time plot (Fig. 4) is essentially linear, it may be assumed that the porosity remains nearly the same during deposition. Thus, assuming a homogeneous coating, the value of coating thickness at the end of the experiment may be divided by the overall duration of experiment to extract the layer's growth rate:

$$\nu = \frac{6100}{2449} = 2.49\ \text{Å/s} \cong 15\ \text{nm/min}. \qquad (5)$$

One may argue that if only an islandlike deposition actually took place, the value of deposit thickness measured by ESEM is not representative, and the related values of apparent density, porosity, and deposition rate are incorrect. Such an argument may arise, for example, because of the XPS data, in which TiO_2 is also noticed. However, the authors feel that this possibility may be excluded based on ellipsometry measurements, which demonstrate uniformity, and AFM images of the uncoated edge of the electrode, which show a distinctly different surface morphology.

At the end of the experiment, $\Delta Q = 272\ \text{mC/cm}^2$ (Fig. 3) and $\Delta m = 57.85\ \mu\text{g/cm}^2$ (Fig. 4) are measured. Hence, using the right-hand-side of Eq. (2), the EW of the deposit material is determined as EW = 20.5 g/equiv. This very low value must reflect either direct electroreduction of the electrolyte or parasitic electrochemical reactions involved in the electrodeposition of OCP. The number of electrons transferred in the reaction(s) forming one mole of a product may be estimated based on the middle term in Eq. (2). Thus, the values listed in Table II for different CaP compounds are obtained. The very high value $n \approx 24$, when assuming OCP, indicates that the OCP is formed via a complex set of reactions and not through a simple electrochemical reaction. Possibly, the electrolysis of water consumes many electrons first, and only when the local pH is increased significantly, the deposition of OCP itself takes place. The importance of identifying the exact CaP formed by electrocrystallization before calculating the value of n is noticeable in Table II, as this value may change from ~7 to ~25, for DCPA and HAp, respectively.

Based on the EQCM data in this work, the number of moles of OCP actually deposited may be estimated; thus, the amount of calcium ions consumed in this process may be determined too. For a mass density $\Delta m = 57.85\ \mu\text{g/cm}^2$ (see Fig. 4), surface area $A = 1.327\ \text{cm}^2$ of the working electrode (see Experimental), and a molecular mass $M_{OCP} = 491.23$ g/mol (see Table II), we estimate that 1.56×10^{-7} mol of OCP is deposited. To achieve this, 6.24×10^{-7} mol of Ca^{2+} are consumed, which, for a 30-mL solution (see Experimental), means 20.8 μM Ca^{2+}. This value is much lower than 0.61 mM of Ca^{2+} initially contained in solution. The dissociation of phosphoric acid at 37°C may be described by means of three-acid dissociation equilibrium constants: $K_{a1} = 5.861 \times 10^{-3}$, $K_{a2} = 6.839 \times 10^{-8}$, and $K_{a3} = 6.607 \times 10^{-13}$.[34,35] The corresponding $pK_i \equiv -\log(K_{ai})$ values are 2.232, 7.165, and 12.18, respectively. Hence, the $\log(\beta_n) \equiv \sum_{i=1}^{n} pK_i$ values are 2.232, 9.397, and 21.577, respectively, where β_n are the equilibrium constants. Thus, phosphoric acid may exist in solution as the neutral molecule or as ions carrying a negative charge of 1–3, depending on pH. The distribution of these species as a function of pH is calculated using the three values of equilibrium constant for an initial concentration 0.36 mM $H_2PO_4^-$, as shown in Figure 10. From this figure, it becomes clear that once a solution containing 0.36 mM $H_2PO_4^-$ at pH 6.0 is prepared, some of the $H_2PO^-_4$ ions deprotonte, forming HPO_4^{2-}. For pH values in the range of 7.2–12.2, the predominant species is HPO_4^{2-}, whereas above pH 12.2 the triply charged anion PO_4^{3-} becomes the most abundant

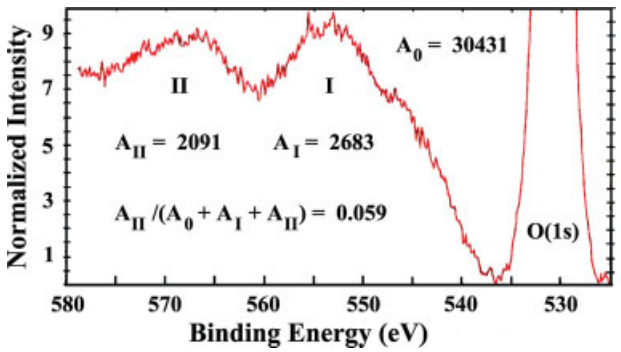

Figure 9. Zoom-in on the shake-up satellite peaks shown in Figure 8. [Color figure can be viewed in the online issue, which is available at www.interscience.wiley.com.]

TABLE II
Experimental XPS Identification of the CaP Phase and the Resulting Value of *n*, as Derived From Eq. (2) Based on EQCM Measurements

	HAp	OCP	DCPA	DCPD	TCP	MCPM	CPP	CPPD
Ca/P, theoretical	1.67	1.33	1.00	1.00	1.50	0.50	1.0	1.00
Ca/P[32]	1.48	1.24	0.93	0.98	1.35	0.48	N/A	N/A
Ca/P, this study	–	1.25	–	–	–	–	–	–
O/Ca[32]	2.76	3.4	4.3	5.4	2.72	10.38	N/A	N/A
O/Ca, this study	–	3.16	–	–	–	–	–	–
$O(1s)_{II}/O(1s)_{total}$[32]	0.065	0.053	0.037	0.020	0.072	0.008	N/A	N/A
$O(1s)_{II}/O(1s)_{total}$, this study	–	0.059	–	–	–	–	–	–
M (g/mol)	502.33	491.23	136.06	172.09	310.18	252.07	254.10	290.13
n (equiv/mol)	24.5	23.9	6.6	8.4	15.1	12.3	12.4	14.1

species. Practically, the concentration of calcium ions in solution is always much higher than the concentration of hydrogen ions, thus statistically allowing the precipitation of CaP in solution, while overcoming the fast kinetics of the phosphate ions recombination with hydrogen ions.

DISCUSSION

Based on Figures 3 and 4, it is concluded that the rate of the CaP deposition reaction is controlled by charge transfer. A charge-transfer reaction, which is said to be under activation control, involves transfer of charge carriers across the double layer. Other possible types of rate control are associated with diffusion (mass transport); chemical reactions on the electrode surface, preceding or following the electron transfer; and adsorption, desorption, or crystallization processes. The present observation of a Faradaic behavior supports the conclusion of Eliaz and Eliyahu[7] that electrochemical reactions are more significant than chemical reactions in the formation of HAp. The present finding that charge transfer, and not diffusion-controlled processes, controls that the reaction rate is also supported by the determination of standard enthalpy of activation. Eliaz et al. measured the mass of HAp on a 1-cm^2 working electrode made of CP-Ti, after 3-h deposition at different temperatures, from a bath composition identical to that used in this work.[8] Plotting their measured data in the form of v versus $1/T$, where v is the deposition rate [g/(h m^2)] and T is the absolute temperature, and comparing to Arrhenius equation

$$\nu = A^* \exp\left(-\frac{\Delta G^{\ddagger}}{RT}\right) \tag{6}$$

the standard enthalpy of activation is estimated to be

$$\Delta H^{\ddagger} \approx 40 \pm 4 \text{ kJ/mol} \tag{7}$$

In Eq. (6), A^* is a pre-exponential factor (also known as frequency factor), R is the ideal gas constant [8.3145 J/(K·mol)], and $\Delta G^{\ddagger} = \Delta H^{\ddagger} - T\Delta S^{\ddagger}$ is Gibbs energy of activation (standard free energy of activation). Equation (6) is derived based on the transition-state theory (also known as the activated complex theory).

It is well accepted that apparent activation energies below ~20 kJ/mol observed in dilute aqueous solutions are indicative of bulk diffusion-controlled processes, whereas those above this value indicate that the reaction kinetics are controlled by the interfacial area.[36] It has also been reported that adsorption of species on the working electrode and subsequent chemical reaction is characterized by an apparent activation energy higher than 43 kJ/mol.[37] For a wide variety of mineral-solution alteration processes, apparent activation energies within the range of 32–80 kJ/mol have been reported.[27,30,38] Thus, it may be concluded that the value of standard enthalpy of activation given in Eq. (7) for electrodeposition of CaP on Ti is reliable, and that a bulk diffusion-controlled process cannot be rate determining. Because

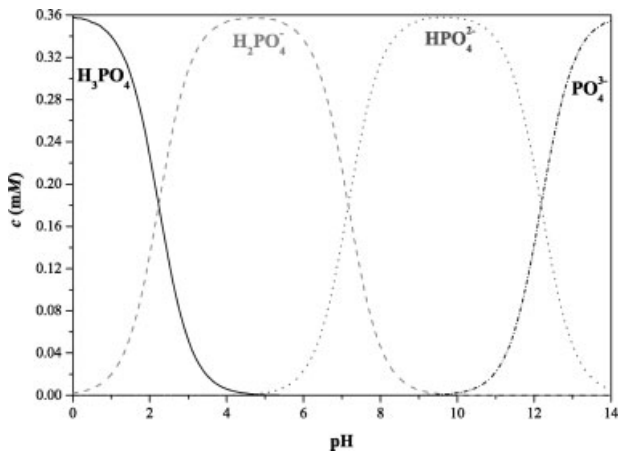

Figure 10. The stepwise deprotonation of phosphoric acid as a function of pH.

no mass gain measurements are conducted after different times of deposition, it is possible that the value of standard enthalpy of activation provided in Eq. (7) is actually an effective value, which is governed by the activation energies of several processes that take place in a sequence. Finally, it should be recalled that the EQCM experiments are carried out at 65°C, for which linear regression of the data by Eliaz et al.[8] predicts deposition rate $v \approx 50$ ng/(cm^2 s). This value is approximately double to that measured directly by EQCM. This difference may be attributed to variation in the deposition conditions, as explained earlier.

Several electrochemical reactions have been considered before[7] and will not be presented here again. Although several of those reactions would lead to a local increase in pH within the diffusion layer, only the electrolysis of water can produce such high current densities, so that no limiting current density is detected in the cyclic voltammograms. Once the proper composition and pH of the electrolyte solution are established in vicinity of the cathode, the following precipitation reactions (among others) may occur:

$$5\,(Ca^{2+}) + 3\,(PO_4^{3-}) + (OH)^- \leftrightarrow HAp \qquad (8)$$

$$4\,(Ca^{2+}) + 3\,(PO_4^{3-}) + H^+ + 2.5H_2O \leftrightarrow OCP \qquad (9.1)$$

or

$$4\,(Ca^{2+}) + 3\,(HPO_4^{2-}) + 2.5\,H_2O \leftrightarrow OCP + 2\,H^+ \qquad (9.2)$$

Comparing reactions (9.1) and (9.2), the latter may have higher probability to actually occur under the studied conditions, because (1) it requires HPO_4^{2-}, not PO_4^{3-}, and therefore does not need the pH to increase as much; and (2) the production of the hydrogen cations partly compensates for the production of hydroxyl ions, thus the increase of pH is slowed down. Inspection of the electrochemical reactions in Ref. 7 does not reveal any set of reactions that actually require $n = 24$ electrons to form one mole of OCP, following either reaction (9.1) or (9.2). Therefore, it is concluded that a large portion of the Faradaic current is consumed by side reactions. The reduction of TiO_2, for example, is beneficial with respect to the activation of the surface of the Ti substrate and attraction of ions toward the surface by electrophoretic forces, thus promoting deposition.

The current transient in Figure 3 is different from the one observed by Eliaz and Eliyahu.[7] This dissimilarity may be associated with different CaP growth morphologies, namely a columnar layer only in this study, when compared with a columnar layer with an underlying layer of nanosized cubical crystals reported earlier.[10] A question then arises, what is the reason for the difference between the current transients in the present as opposed to the previous work of Eliaz et al. The answer is, most likely, the variation of the experimental conditions during deposition. In the previous work, current transients were acquired in a macrocell, at $T = 80$–85°C, $E = -1.4$ V versus SCE, and the surface of the working electrode (ground and polished CP-Ti grade 2) having a vertical orientation. In this work, on the other hand, the current transients are acquired in the EQCM cell, at $T = 65$°C, $E = -1.29$ V versus SCE, and the surface of the working electrode (vapor-deposited Ti) having a horizontal orientation. Moreover, the deposition on the EQCM electrode begins after it has been immersed in the electrolyte solution for more than an hour in the framework of the stability test. It is well known that changes in the surface state of the substrate, in the overpotential, and in the solution concentration close to the surface may all affect the shape of the current transient significantly. It cannot be excluded, for example, that the adsorption of specific ions on the surface of the electrode during the stability test modifies the initial conditions for deposition.

The incubation time observed in the Δm versus time plot (Fig. 4) is similar to that observed earlier[26,27] and may be related to the occurrence of side reactions that increase the local pH, thus promoting the formation of OCP, in accordance with Figure 10. To support this hypothesis, further EQCM experiments should be carried out with the same ion concentrations, but adjusted to different pH values. It is anticipated that with the increase of pH, the incubation time will be shortened. In addition, it should become more probable to form HAp coatings at higher Faradaic efficiencies.

The next issue to be discussed is that of the formation of OCP as a precursor to HAp. It was Ostwald, who first suggested that upon phase transformation, whether crystallization, melting, or condensation, the phase that nucleates first is not necessarily the thermodynamically most stable one, but that with free energy, which is closest to the original state.[39] This statement has become known as "Ostwald's rule." In agreement with this rule, it has been suggested that several CaP phases, such as OCP, DCPD, and ACP, may serve as precursors to the formation of HAp *in vivo*.[2,40,41] The OCP phase has triclinic crystallographic structure (space group $P\bar{1}$) and consists of alternating apatitic and hydrated layers, which are stacked together parallel to their (100) plane. Therefore, it was suggested that the transformation of OCP into HAp may proceed via: (1) a process of OCP dissolution and reprecipitation of HAp crystals

and (2) *in situ* hydrolysis that is accompanied by calcium consumption from the surrounding solution and release of phosphate ions into the solution.[41] Wang et al. also found that during early stage mineralization ($\leq$7 d) in canine trabecular bone of dogs, the Ca/P ratio in the mineralized tissue adjacent to the electrodeposited HAp coating resembled that in OCP, although DCPD or ACP could not be excluded.[10] As precipitation of OCP may occur in the presence of either HPO_4^{2-}or PO_4^{3-} [see Eqs. (9.1) and (9.2)], whereas precipitation from solution of HAp requires a supersaturated concentration of PO_4^{3-} to be established first [see Eq. (8)], it may be expected that OCP will form within a lower pH range compared to HAp. Indeed, it has been reported that in aqueous solutions at 25°C, the pH-stability ranges for OCP and HAp are 5.5–7.0 and 9.5–12.0, respectively.[1]

The very high value of pH that is required to favor the formation of $PO_4^{3-}$by chemical reactions, according to Figure 10, is obviously unattainable *in vivo*. Therefore, the following conclusions may be drawn: (1) the formation of either OCP or HAp may not be under simple chemical equilibrium conditions, but instead be controlled largely by electrochemical process that increase the local concentration of phosphate ions. (2) The solubility product K_{sp}, which is equal to the ion activity product at equilibrium, must be very low, to allow precipitation of CaP even at relatively low concentrations of calcium and phosphate/hydrogen phosphate ions. Indeed, pK_{sp} values of 47.08 and 58.6 have been reported for OCP and HAp at 37°C, respectively.[35] It is well known that CaP salts are only sparingly soluble in aqueous solutions. (3) It is more likely for HAp to form via transformation of precursor phases, such as OCP, rather than directly. In this investigation, this precursor is clearly identified. We assume that, in those studies, where no precursor was observed, the reason may be either its morphological and structural similarity to HAp (in the case of OCP), conversion over time to the more stable HAp, or the use of insensitive analytical techniques for the determination of the chemical composition of the coating just at the interface with the substrate. (4) The precipitation from solution of CaP may take place only within a very small volume adjacent to the surface of the substrate.

CONCLUSIONS

EQCM data acquired *in situ* and in real time allows for analyzing the time dependence of the current transient and mass gain during electrocrystallization of CaP onto pure Ti. In combination with advanced XPS chemical analysis, AFM, and ESEM imaging, the following conclusions are drawn:

1. Except for a short incubation time, the process by which the CaP is formed is found to follow a Faradaic behavior, thus demonstrating the important role that charge transfer plays. The incubation time may be related to the need for local increase of pH before precipitation from solution can take place.
2. The deposition process is characterized by a rate of 23.5 ng/(cm^2 s) or 15 nm/min. The high-EW value of 20.5 g/equiv, and the associated remarkably high number of electrons transferred in the reaction $n \sim 24$, indicates that most of the current is consumed either by electrolysis of water or by a complex set of parasitic reactions.
3. Based on macroscopic, three-electrode cell measurements, the standard enthalpy of activation is ~40 kJ/mol. This high value is typical of interfacial reactions and indicates that diffusion in the bulk solution does not play a major role in the electrocrystallization process.
4. Analysis of the integrated intensity of the oxygen shake-up peaks in the XPS spectra, in combination with the determination of Ca/P and O/Ca atomic ratios, allows for identifying that OCP was deposited on the Ti electrode. This phase plays an important role as a precursor to HAp during *in vivo* biomineralization too.
5. The OCP layer is found to be ~0.61 μm thick and has an apparent density of 0.95 g/cm^3, thus reflecting a high porosity of 63.6%, which may be useful as a scaffold for bone ingrowth.
6. Calculations based on acid dissociation equilibrium constants and solubility products indicate that HAp may most likely form via transformation of precursor phases, such as OCP, rather than directly. The very low solubility product allows precipitation of CaP even at relatively low concentrations of calcium and phosphate/hydrogen phosphate ions.
7. The EQCM can provide valuable information on the nucleation and growth of different CaP phases due to chemical or electrochemical reactions, far beyond its use a sensitive balance.

The authors are grateful to E. Gileadi for fruitful scientific discussions, peer review of this work, and wise advices. We are also thankful to the Japanese Society for the Promotion of Science (JSPS), Asian and African Science Platform Program, for its 3-year financial support that enabled, among others, the visit and work of W. Kopelovitch at the Institute of Biomaterials and Bioengineering, Tokyo Medical and Dental University. The authors also thank Z. Barkay from the Wolfson Applied Materials Research Centre for the ESEM study and both M. Levinshtein and M. Eliyahu for the AFM study.

References

1. Dorozhkin SV, Epple M. Biological and medical significance of calcium phosphates. Angew Chem Int Ed 2002;41:3130–3146.
2. Johnsson MSA, Nancollas GH. The role of brushite and octacalcium phosphate in apatite formation. Crit Rev Oral Biol Med 1992;3:61–82.
3. Darimont GL, Gilbert B, Cloots R. Non-destructive evaluation of crystallinity and chemical composition by Raman spectroscopy in hydroxyapatite-coated implants. Mater Lett 2003;58: 71–73.
4. Overgaard S, Lind M, Josephsen K, Maunsbach AB, Bünger C, Søballe K. Resorption of hydroxyapatite and fluorapatite ceramic coatings on weight-bearing implants: A quantitative and morphological study in dogs. J Biomed Mater Res 1998; 39:141–152.
5. Gineste L, Gineste M, Ranz X, Ellefterion A, Guilhem A, Rouquet N, Frayssinet P. Degradation of hydroxylapatite, fluoroapatite, and fluorhydroxyapatite coatings of dental implants in dogs. J Biomed Mater Res 1999;48:224–234.
6. Wenisch S, Stahl JP, Horas U, Heiss C, Kilian O, Trinkaus K, Hild A, Schnettler R. In vivo mechanisms of hydroxyapatite ceramic degradation by osteoclasts: Fine structual microscopy. J Biomed Mater Res A 2003;67:713–718.
7. Eliaz N, Eliyahu M. Electrochemical processes of nucleation and growth of hydroxyapatite on titanium supported by real-time electrochemical atomic force microscopy. J Biomed Mater Res A 2007;80:621–634.
8. Eliaz N, Sridhar TM, Rosenberg Y. Electrodeposition of hydroxyapatite on titanium for implants. In: Lütjering G, Albrecht J, editors. Proceedings of the 10th World Conference on Titanium, Vol. 5. Weinheim, Germany: Wiley-VCH; 2004. p 3299–3306.
9. Eliaz N, Sridhar TM, Mudali UK, Raj B. Electrochemical and electrophoretic deposition of hydroxyapatite for orthopaedic applications. Surf Eng 2005;21:238–242.
10. Wang H, Eliaz N, Xiang Z, Hsu HP, Spector M, Hobbs LW. Early bone apposition in vivo on plasma-sprayed and electrochemically deposited hydroxyapatite coatings on titanium alloy. Biomaterials 2006;27:4192–4203.
11. Sauerbrey G. Use of vibrating quartz for thin film weighing and microweighing. Z Phys 1959;155:206–222 (in German).
12. Daikhin L, Gileadi E, Tsionsky V, Urbakh M, Zilberman G. Slippage at adsorbate-electrolyte interface. Response of electrochemical quartz crystal microbalance to adsorption. Electrochim Acta 2000;45:3615–3621.
13. Kanazawa KK, Gordon JG. The oscillation frequency of a quartz resonator in contact with a liquid. Anal Chim Acta 1985;175:99–105.
14. Lori JA, Hanawa T. Characterization of adsorption of glycine on gold and titanium electrodes using electrochemical quartz crystal microbalance. Corr Sci 2001;43:2111–2120.
15. Marx KA. Quartz crystal microbalance: A useful tool for studying thin polymer films and complex biomolecular systems at the solution-surface interface. Biomacromolecules 2003;4:1099–1120.
16. Ward MD. Principles and applications of the electrochemical quartz crystal microbalance. In: Rubinstein I, editor. Physical Electrochemistry: Principles, Methods and Applications, Vol. 7. New York: Marcel Dekker; 1995. p 293–338.
17. Buttry DA, Ward MD. Measurement of interfacial processes at electrode surfaces with the electrochemical quartz crystal microbalance. Chem Rev 1992;92:1355–1379.
18. Tsionsky V, Daikhin L, Urbakh M, Gileadi E. Looking at the metal/solution interface with the electrochemical quartz crystal microbalance: Theory and experiment. In: Bard AJ, Rubinstein I, editors. Electroanalytical Chemistry: A Series of Advances, Vol. 22. New York: Marcel Dekker; 2004. p 1–99.
19. Urbakh M, Tsionsky V, Gileadi E, Daikhin L. Probing the solid/liquid interface with the quartz-crystal microbalance. In: Steinem C, Jonshoff A, editors. Piezoelectric Sensors. Berlin, Heidelberg: Springer; 2007. p 111–150.
20. Jones DA. Principles and Prevention of Corrosion. New York: Macmillan Publishing Company; 1992. pp 75–76.
21. Zhu Z, Tong H, Jiang T, Shen X, Wan P, Hu J. In situ monitoring the growth of hap crystal on the surface of Ti/TiO_2 in SBF with a quartz crystal microbalance. Key Eng Mater 2007;330–332:717–720.
22. Monkawa A, Ikoma T, Yunoki S, Yoshioka T, Tanaka J, Chakarov D, Kasemo B. Fabrication of hydroxyapatite ultra-thin layer on gold surface and its application for quartz crystal microbalance technique. Biomaterials 2006;27:5748–5754.
23. Zhu Z, Tong H, Jiang T, Shen X, Wan P, Hu J. Studies on induction of L-aspartic acid modified chitosan to crystal growth of the calcium phosphate in supersaturated calcification solution by quartz crystal microbalance. Biosens Bioelectr 2006;22:291–297.
24. Zhu P, Masuda Y, Yonezawa T, Koumoto K. Investigation of apatite deposition onto charged surfaces in aqueous solutions using a quartz-crystal microbalance. J Am Ceram Soc 2003;86: 782–790.
25. Okido M, Kuroda K, Ichino R. Formation of calcium phosphate film on Ti substrate in aqueous solutions in the control of temperature and ion activity. Mater Sci Forum 2003;426–432:3457–3461.
26. Okido M, Nishikawa K, Kuroda K, Ichino R, Zhongwei Z, Takai O. Evaluation of the hydroxyapatite film coating on titanium cathode by QCM. Mater Trans 2002;43:3010–3014.
27. Ban S. Real-time monitoring of apatite deposition using electrochemical quartz crystal microbalance. Dent Mater J 2003; 22:467–474.
28. Zhu PX, Masuda Y, Koumoto K. Site-selective adhesion of hydroxyapatite microparticles on charged surfaces in a supersaturated solution. J Colloid Interf Sci 2001;243:31–36.
29. Tanahashi M, Matsuda T. Surface functional group dependence on apatite formation on self-assembled monolayers in a simulated body fluid. J Biomed Mater Res 1997;34:305–315.
30. Tanahashi M, Kokubo T, Matsuda T. Quantitative assessment of apatite formation via a biomimetic method using quartz crystal microbalance. J Biomed Mater Res 1996;31:243–249.
31. Brown WE, Chow LC. Chemical properties of bone mineral. Annu Rev Mater Sci 1976;6:213–236.
32. Lu HB, Campbell CT, Graham DJ, Ratner BD. Surface characterization of hydroxyapatite and related calcium phosphates by XPS and TOF-SIMS. Anal Chem 2000;72:2886–2894.
33. Chusuei CC, Goodman DW, Van Stipdonk MJ, Justes DR, Schweikert EA. Calcium phosphate phase identification using XPS and time-of-flight cluster SIMS. Anal Chem 1999;71:149–153.
34. Sillén LR, Martell AE. Stability Constants of Metal-Ion Complexes. London: The Chemical Society; 1964.Supplement 17, p 180–181.
35. Koutsoukos P, Amjad Z, Tomson MB, Nancollas GH. Crystallization of calcium phosphates. A constant composition study. J Am Chem Soc 1980;102:1553–1557.
36. Laidler KJ. Chemical Kinetics. New York: McGraw-Hill; 1958.
37. Soliman HMA, Abdel-Rahman HH. The use of rotating cylinder electrode to study the effect of 1,3-dihydroxypropane on the production of copper powder. J Braz Chem Soc 2006;17: 705–714.
38. Lasaga AC. Kinetic Theory in the Earth Sciences. New Jersey: Princeton University Press; 1997.
39. Ostwald W. The formation and changes of solids. Z Phys Chem 1897;22:289–302 (in German).
40. Brown WE, Eidelman N, Tomazic B. Octacalcium phosphates as a precursor in biomineral formation. Adv Dent Res 1987;1: 306–313.
41. Suzuki O, Kamakura S, Katagiri T. Surface chemistry and biological responses to synthetic octacalcium phosphate. J Biomed Mater Res B 2006;77:201–212.